

Colliding localized, lumpy holographic shocks with a granular nuclear structure

Sebastian Waeber,^a Laurence G. Yaffe^b

^a*Department of Physics, Technion, Haifa 32000, Israel*

^b*Department of Physics, University of Washington, Seattle WA 98195-1560, USA*

E-mail: wsebastian@campus.technion.ac.il,
yaffe@phys.washington.edu

ABSTRACT: We apply a recent and simple technique which speeds up the calculation of localized collisions in holography to study more realistic models of the pre-hydrodynamic phase of heavy ion collisions using gauge/gravity duality. Our initial data reflects the lumpy nuclear structure of real heavy ions and our projectiles' aspect ratio mimics the Lorentz contraction of nuclei during RHIC collisions. At the hydrodynamization time of the central region of the quark gluon plasma developed during the collision, we find that most of the system's vorticity is located well outside the hydrodynamized part of the plasma. Only the relativistic corrections to the thermal vorticity within the hydrodynamized region are non-negligible. We compare the transverse flow shortly after the collision with previous results which did not use granular initial conditions and determine the proper energy density and fluid velocity in the hydrodynamized subregion of the plasma.

KEYWORDS: holography, gravitational shockwaves, quark-gluon plasmas, heavy ion collision, numerical relativity

Contents

1	Introduction	1
2	Initial data and nuclear model	4
3	Time evolution	7
4	Results	8
4.1	Boundary stress energy tensor	8
4.2	Hydrodynamization	12
4.3	Vorticity	16
5	Conclusion	21

1 Introduction

Numerical calculations of holographic models of heavy ion collisions, via high-accuracy solutions of five-dimensional Einstein equations [1], require very substantial calculational resources in both run-time and memory if the initial data is chosen to closely mimic the energy density of incoming nuclei in heavy ion collisions at, e.g., RHIC. Holographic calculations to date, despite using initial data modeling simplified and rather unrealistic descriptions of real nuclei, have yielded insight into significant aspects of the early phase of heavy ion collisions including the onset of hydrodynamic behavior, the domain of validity of hydrodynamic descriptions, pre-hydro development of radial and transverse flow, near-universal rapidity dependence, and more [1–9]. However, many interesting questions involving the early phase of quark-gluon plasma dynamics remain unexplored, impeded by the computational challenges involved in solving 5D Einstein equations in geometries with no dimensionality-reducing symmetries and with spatio-temporal structure whose accurate representation requires a very large dynamic range. Some of these questions, not yet adequately explored, include the effect of initial state fluctuations on the formation and early stage dynamics of produced quark-gluon plasma, the interplay between energy density fluctuations and dependence on charge and flavor densities, and the evolution of plasma vorticity, as well as the effect of finite t Hooft coupling corrections needed to more closely model real QCD.

In this work we focus on enabling holographic modeling of early stage heavy ion collisions with initial data which closely mimics the granular structure of real nuclei. The underlying dual field theory is the strong coupling limit of maximally supersymmetric Yang-Mills theory ($\mathcal{N}=4$ SYM), not real QCD for which no correct dual holographic description is known. In other words, we are approximating the dynamics of quark-gluon plasma (QGP) produced in real heavy ion collisions, a highly relativistic and strongly coupled non-Abelian plasma, by the dynamics of $\mathcal{N}=4$ SYM plasma in its strong coupling (and large N_c) limit. This, to be sure, is a drastic approximation. As $\mathcal{N}=4$ SYM is a conformal theory, unlike QCD, trying to model QCD using $\mathcal{N}=4$ SYM completely eliminates all dynamics related to hadronization and actual particle production. At best, holographic models based on $\mathcal{N}=4$ SYM can mimic the behavior of real QGP during early stages of a collision where the quark-gluon plasma does behave like a near-conformal fluid.¹

In assessing the utility of holographic modeling of heavy ion collisions, one should bear in mind that available alternative treatments for modeling early stage dynamics in these collisions make at least equally large approximations. Many studies have used a Glauber model of the initial projectile energy densities directly as hydrodynamic initial data, as if there were no non-trivial pre-hydrodynamic evolution whatsoever [10, 11]. Much effort has also been devoted to studying *asymptotically* high energy collisions, leading to the development of the Color Glass Condensate (CGC) description of collisions which may be viewed as involving high occupancy of very weakly coupled partons [12]. This asymptotic regime, with a plethora of scales differing by powers of the weak coupling, is far from what is achievable in experimentally accessible collisions. Modeling which uses a CGC-inspired treatment of the initial state to generate initial data for hydrodynamic evolution amounts to converting, instantly, from an asymptotically weakly coupled description to a near-ideal fluid description in which microscopic constituents are strongly interacting and correlation lengths are shorter than any other relevant scale. This is intrinsically inconsistent, but reflects the reality that there are no fully controlled calculational techniques for studying the dynamics of real QGP as produced in current experiments.

Holographic modeling based on $\mathcal{N}=4$ SYM provides a description of early stage dynamics which incorporates, correctly, the strong-coupling dynamics of a not-quite QCD non-Abelian plasma. The resulting treatment is complementary to CGC-inspired models that involve extrapolations of asymptotically weak coupling descriptions to experimentally accessible collisions in which the produced plasma is not weakly coupled.

¹There are non-conformal theories with known holographic descriptions some of which, while still differing from QCD, might be suitable for providing more controlled models of hadronization. Addressing such late-stage dynamics is outside the scope of the present work.

For the remainder of this paper, we take as given this motivation for using holographic modeling based on $\mathcal{N} = 4$ SYM to study early stages of relativistic heavy ion collisions.²

While the earlier holographic calculation in [1] captured qualitative features of a collision of projectiles somewhat resembling colliding nuclei, the aspect ratios of the projectiles considered in [1] were an order of magnitude smaller than the aspect ratios of (lab frame) Lorentz contracted nuclei in RHIC collisions. The resource requirements (in both run time and memory) of the most demanding steps in computing these collision, without resorting to any computational approximations, increase approximately quadratically with increasing aspect ratios. However, if one hopes to make quantitative statements about observables that are sensitive to the ratio between the transverse and longitudinal scales, such as the vorticity, it is necessary to work with projectiles with realistic Lorentz contractions. Moreover, there is compelling evidence that transverse fluctuations in the energy densities of colliding nuclei have large influence on the resulting plasma evolution and, in particular, that strong fluctuations are necessary to account for the size of odd azimuthal flow moments v_{2i+1} observed in experiments [13, 14]. These flow moments $\{v_n\}$ are the Fourier expansion coefficients (in azimuthal angle) of the transverse plane particle distribution,

$$E \frac{d^3 N}{dp^3} = \frac{1}{2\pi} \frac{d^2 N}{p_T dp_T dy} \left(1 + 2 \sum_{n=0}^{\infty} v_n \cos(n(\phi - \Psi_n)) \right), \quad (1.1)$$

with E the energy, p momentum, p_T transverse momentum, ϕ the azimuthal angle, y the pseudorapidity of a final state particle, and Ψ_n the n -th harmonic symmetry plane angle [15]. The observation of large odd moments, which would be suppressed if the overlap region of the projectiles during the collision was perfectly smooth, imply strong transverse fluctuations [14].

In the present work, our goal is to demonstrate the feasibility of computing holographic collisions with initial data modeling far more realistic collisions than has previously been possible, and examine the resulting implications for the onset of hydrodynamic behavior as well as the development of pre-hydrodynamic flow and vorticity. In particular, we will incorporate initial state fluctuations in energy density along the lines of the treatment in [10, 11], and an aspect ratio of our projectiles which matches the Lorentz contraction of RHIC collisions.

Attempting to perform this calculation using exactly the same calculational techniques employed in [1], involving a characteristic formulation of Einstein's equations,

²There are, of course, important probes of heavy ion collisions involving high transverse momentum jets and produced particles for which holographic modeling is not appropriate. The goal of holographic modeling is to capture the dynamics of the bulk of the produced plasma, not high momentum tails of distributions for which the asymptotic freedom of QCD is essential.

spectral approximations for the resulting partial differential equations, and relying a sufficiently large non-distributed unitary memory system, would not be feasible – at least on systems to which we have full-time access. To make this calculation feasible, we will employ the transverse derivative expansion procedure developed in [16]. As shown in that work, expanding in transverse derivatives produces a simple, yet effective technique for computing approximate but quite accurate solutions to localized holographic collisions. By expanding in transverse gradients up to first order in derivatives we could reproduce the exact solutions, for intervals up to the hydrodynamization time, to within errors in the range of 1-10%, using only a small fraction of the run-time and memory that would be needed for the exact calculation with no expansion in transverse gradients.

We will apply this technique to compute, via holography, the collision of projectiles with a lumpy, granular structure, reflecting the nuclear structure of heavy ions. For the initial data we use a Lorentz-contracted Woods-Saxon potential as the probability distribution of the centers of the individual nucleons. The Lorentz contraction factor will reflect energies at RHIC collisions. We enforce a minimal distance of the nucleons' centers to ensure limited overlap as in [10, 11]. The nuclear model giving rise to our holographic initial data also takes into account a realistic skin thickness of the nuclei.

We will find that the time at which roughly half of the central, low rapidity region can be described by hydrodynamics approximately corresponds to the hydrodynamization time of the same region observed during collisions of smooth Gaussians without a lumpy structure. This is in line with the expectations from [24], which predicted that granular initial data should delay full hydrodynamization by about a factor of 2. The vorticity, at the time when the majority of the central region of the quark gluon plasma has hydrodynamized, is dominated by contributions far away from the central region, with only a small fraction of the vorticity in the system deposited in the hydrodynamized center. The calculation presented in this work is a natural extension of the model discussed in [4], where the authors approximated heavy ions by smooth Woods-Saxon potentials, studied central collisions via planar shockwave collisions in holography, and only included transverse dynamics later on in the hydrodynamic evolution.

2 Initial data and nuclear model

Following [1–3], we first formulate the metric for a single shockwave in AdS₅ using Fefferman-Graham coordinates,

$$ds_{FG}^2 = \frac{1}{\rho^2} \left(-dt^2 + d\rho^2 + (d\mathbf{x}^\perp)^2 + dz^2 + \rho^4 h_\pm(\mathbf{x}^\perp, z^\mp, \rho) (dz^\pm)^2 \right), \quad (2.1)$$

with $z^\mp = z \mp t$, and ρ an inverted radial coordinate. The Einstein equations require

$$\left(\frac{d^2}{d\rho^2} - \frac{3}{\rho} \frac{d}{d\rho} + \nabla_\perp^2\right)\rho^4 h_\pm = 0. \quad (2.2)$$

In the dual quantum field theory, the metric (2.1) corresponds to a state with

$$\langle T^{00} \rangle = \langle T^{zz} \rangle = \frac{N_c^2}{2\pi^2} h_\pm \Big|_{\rho=0}, \quad (2.3a)$$

$$\langle T^{0z} \rangle = \pm \frac{N_c^2}{2\pi^2} h_\pm \Big|_{\rho=0}. \quad (2.3b)$$

Due to the large aspect ratios of the Lorentz contracted projectiles, longitudinal gradients are much larger than transverse spatial gradients. To simplify the problem we exploit this separation of scales by systematically expanding the Einstein equations in transverse derivatives. We use the symbol $\mathcal{O}(\nabla_\perp^i)$ to represent terms that are at least of i -th order in transverse derivatives. (This is explained in more detail in the Appendix.)

Through first order in transverse derivatives, the single shock function h_\pm has no radial dependence

$$h_\pm(\mathbf{x}^\perp, z^\mp, \rho) = h_\pm(\mathbf{x}^\perp, z^\mp) + \mathcal{O}(\nabla_\perp^2). \quad (2.4)$$

Otherwise (2.2) does not constrain $h_\pm(\mathbf{x}^\perp, z^\mp)$ as a function of boundary coordinates, so it may be chosen to be an arbitrary function of \mathbf{x}^\perp and z^\mp . We aim to choose h_\pm so that the initial boundary stress energy tensor corresponds to a realistic model for a boosted gold nucleus. The model we use is motivated by the standard model for heavy ions usually applied in Glauber Monte Carlo simulations [10, 11]. There the position of each nucleon in the nucleus is determined from a probability density function that can be thought of as the single-particle probability density in a quantum mechanical model. We take this probability density to be a boosted spherically symmetric distribution. The radial distribution is derived from low energy electron scattering experiments [17] and is given by a boosted Fermi distribution with three shape parameters: the nuclear radius R , the skin thickness a , and the boost factor γ . The resulting probability distribution for the position of a nucleon is a standard Woods-Saxon potential,

$$P(\mathbf{x}^\perp, z^\mp) = \frac{n}{1 + \exp\left(\left(\sqrt{(x^\perp)^2 + \gamma^2(z^\mp)^2} - R\right)/a\right)}. \quad (2.5)$$

The normalization constant n is chosen such that $\int dx^3 P = 1$. To model RHIC collisions, we use $\gamma = 100$ as the longitudinal Lorentz contraction factor of each colliding nucleus. The energy density of each nucleon is modeled as a Lorentz-contracted Gaus-

sian profile,

$$G_{\pm}(\mathbf{x}^{\perp}, z^{\mp}, \mathbf{x}_0^{\perp}, z_0^{\mp}) = \frac{\mu^3}{\sqrt{2\pi w^2/\gamma^2}} \exp\left(-\frac{\gamma^2}{2}(z^{\mp} - z_0^{\mp})^2/w^2\right) \exp\left(-\frac{1}{2}(\mathbf{x}^{\perp} - \mathbf{x}_0^{\perp})^2/w^2\right), \quad (2.6)$$

centered around $(\mathbf{x}_0^{\perp}, z_0^{\mp})$, with the same Lorentz-contraction as in the nucleon distribution (2.5). To ensure that the individual nucleons have limited overlap, we follow [10, 11] and implement a minimal distance d_{\min} between them. We do so by generating the ensemble of nucleon centers in the following way: after choosing the i -th nucleon center point $(\mathbf{x}_i^{\perp}, z_i^{\mp})$, we update the probability distribution (2.5) via

$$P \rightarrow P \times \Theta(|\mathbf{x}^{\perp} - \mathbf{x}_i^{\perp}|^2 + \gamma^2(z^{\mp} - z_i^{\mp})^2 - d_{\min}^2), \quad (2.7)$$

with Θ a unit step function. We repeat this procedure after each chosen nucleon center. The projectile energy density function h_{\pm} is then given by the superposition

$$h_{\pm}(\mathbf{x}^{\perp}, z^{\mp}) = \sum_{i=0}^{196} G_{\pm}(\mathbf{x}^{\perp}, z^{\mp}, \mathbf{x}_i^{\perp}, z_i^{\mp}). \quad (2.8)$$

Since we aim to simulate heavy ion collisions with realistic parameters, we choose (as in, e.g., [4]) the scale μ determining the the amplitude of G_{\pm} such that

$$\frac{N_A \times 200 \text{ GeV}}{2} = E_{\text{RHIC}} = \int d^2\mathbf{x}_{\perp} dz \langle T^{00} \rangle = \frac{N_c^2}{2\pi^2} \int d^2\mathbf{x}_{\perp} dz h_{\pm} \Big|_{\rho=0}, \quad (2.9)$$

with $N_A = 197$ being the number of nucleons in a gold nucleus and $N_c = 3$ the gauge group rank of QCD. After choosing the skin thickness of the potential a , the minimal distance d_{\min} , the transverse size of each nucleon w , and the transverse size R of the probability distribution (2.5) in units of $[1/\mu]$, the condition (2.9) then fixes the amplitude μ in (2.6) and allows us to give R , a , d_{\min} , and w in units of $[1/\text{GeV}]$.

We work with a nuclear model using the following parameters. As in [4] the transverse size R of our probability distribution (2.5) is 6.5 fm, and the skin thickness is set to 0.66 fm; these values are close to nuclear parameters obtained from elastic electron scattering [18]. The minimal distance $d_{\min} = 0.4$ fm, as in [11], and each nucleon has transverse size $w = 1$ fm. These parameters lead to the value $\mu = 1.1$ GeV. Our nucleon size w is larger than the typical nucleon size of $w \approx 0.5$ fm argued for in [30]. We use a somewhat larger nucleon size since it decreases the required longitudinal and transverse resolution and speeds up the computation. It should be noted that since our nucleons themselves are Gaussian energy density distributions, the actual skin thickness of the heavy ion model and the skin thickness a of the probability distribution (2.5) are not

identical. Therefore we compute multiple ensembles of initial data following the above procedure, for various choices of a in (2.5). We then select the ensemble whose average possesses an actual skin thickness of 0.66 fm and select two random samples from this ensemble, corresponding to left and right moving shocks. With our choice for μ the parameter a in (2.5) is 0.165 fm.

For the numerical evolution we work in units such that the longitudinally integrated energy density profile of a single nucleus at vanishing transverse radius is normalized to one,

$$\int dz h_{\pm}(\mathbf{x}^{\perp}=0) = 1. \quad (2.10)$$

We then use the above parameter values to present results in physical units.

To construct initial data for the time evolution in a coordinate system in which one can employ the characteristic formulation of general relativity, it is necessary to transform the metric ansatz (2.1) on the initial time slice from Fefferman-Graham coordinates to infalling Eddington-Finkelstein coordinates, for which the metric has the form

$$ds_{EF}^2 = u^{-2} \left(g_{\mu\nu}^{EF}(x, r) dx^{\mu} dx^{\nu} - 2 dr du \right). \quad (2.11)$$

We perform this transformation order by order in transverse derivatives following the method outlined in [1–3, 16]. To compute the coordinate transformation numerically we discretize spacetime and use Fourier grids in spatial directions with $N_x = N_y = 40$ and $N_z = 256$ grid points, and a Chebyshev grid in the radial direction with three domains and $N_u = 3 \times 28$ grid points in total. In [16], we show in detail how to construct initial data as an expansion in transverse derivatives. We choose an impact parameter \vec{b} along the x direction with $|\vec{b}| = 4.5$ fm.

3 Time evolution

To compute time evolution we expand the Einstein equations in transverse derivatives and solve them order by order on each time slice through first order in transverse gradients. We briefly review the main idea behind the transverse derivative expansion in the Appendix. A more thorough discussion of this expansion technique and how to efficiently solve the transverse derivative expanded Einstein equations may be found in [16]. As shown there, the approximation by a truncated expansion in transverse gradients for collisions of shocks with large aspect ratios provides substantial run time and memory improvements, while errors are $\lesssim 10\%$ at the hydrodynamization time. On each time slice one has to solve an elliptic partial differential equation to ensure that the radial position of the horizon remains stationary [2]. By expanding in transverse

gradients, this equation simplifies from an elliptic differential equation to a collection of ordinary differential equations in the longitudinal coordinate. This simplification is a major contributor to the above-mentioned calculational improvements.

To solve the expanded Einstein equations numerically, we use a two-domain Chebyshev grid with $N_u = 2 \times 21$ grid points in radial direction of the AdS space and Fourier grids with $N_x = N_y = 40$ and $N_z = 256$ in spatial directions. Time evolution of the geometry is performed using a fourth order Runge-Kutta algorithm with a physical time step size of $\delta t = 7.5 \times 10^{-4}$ fm/ c . Just using a Mathematica implementation running on a decade-old multi-core desktop computer with 128 Gb of memory, we solve the geometry from $t_0 = -0.144$ fm/ c to $t_1 = 0.144$ fm/ c in about three weeks of run time.³ The initial projectiles have coinciding longitudinal positions at time $t = 0$. The initial time $t_0 = -0.144$ fm/ c is chosen such that the single shock bulk solutions in the dual gravity theory do not overlap within the integration domain. The integration domain stretches between the boundary and the apparent horizon of a smooth Schwarzschild black brane which is always present in the two-shock geometry. To improve numerical stability, we add a small uniform background energy density equal to 7% of the peak energy density of the individual projectiles. This background energy density has only minimal influence on the evolution during the period we study.

4 Results

4.1 Boundary stress energy tensor

Using the gauge/gravity dictionary, we determine the boundary stress energy tensor from the near boundary expansion of the bulk metric. Figure 1 depicts the energy density at 0.144 fm/ c before the collision, at the time of the collision $t = 0$ and at 0.068 fm/ c and 0.144 fm/ c after the collision, where we chose $t = 0$ as the time when the center of masses of the projectiles are located at the same longitudinal coordinate. At the time of the collision, $t = 0$, the maximum energy density has reached 160% of the peak energy density of an initial projectile. Due to the granularity of the initial data, the overall maximum energy density is not reached exactly at $t = 0$, but at $t = 0.034$ fm/ c after the collision and measures 170% of the initial peak energy density. At $t = 0$, similar to what is observed during planar collisions and in [1], the energy density profile matches to a good accuracy (with an error of approximately 0.15%) the superposition of the two initial shocks. The second row of figures in Fig. 1 shows the energy density at times 0.068 fm/ c and 0.144 fm/ c after the collision. The maximum of the energy density on those times slices has decreased to 107% and 50% of the initial peak energy

³On newer machines with the same total memory, our codes run approximately twice as fast.

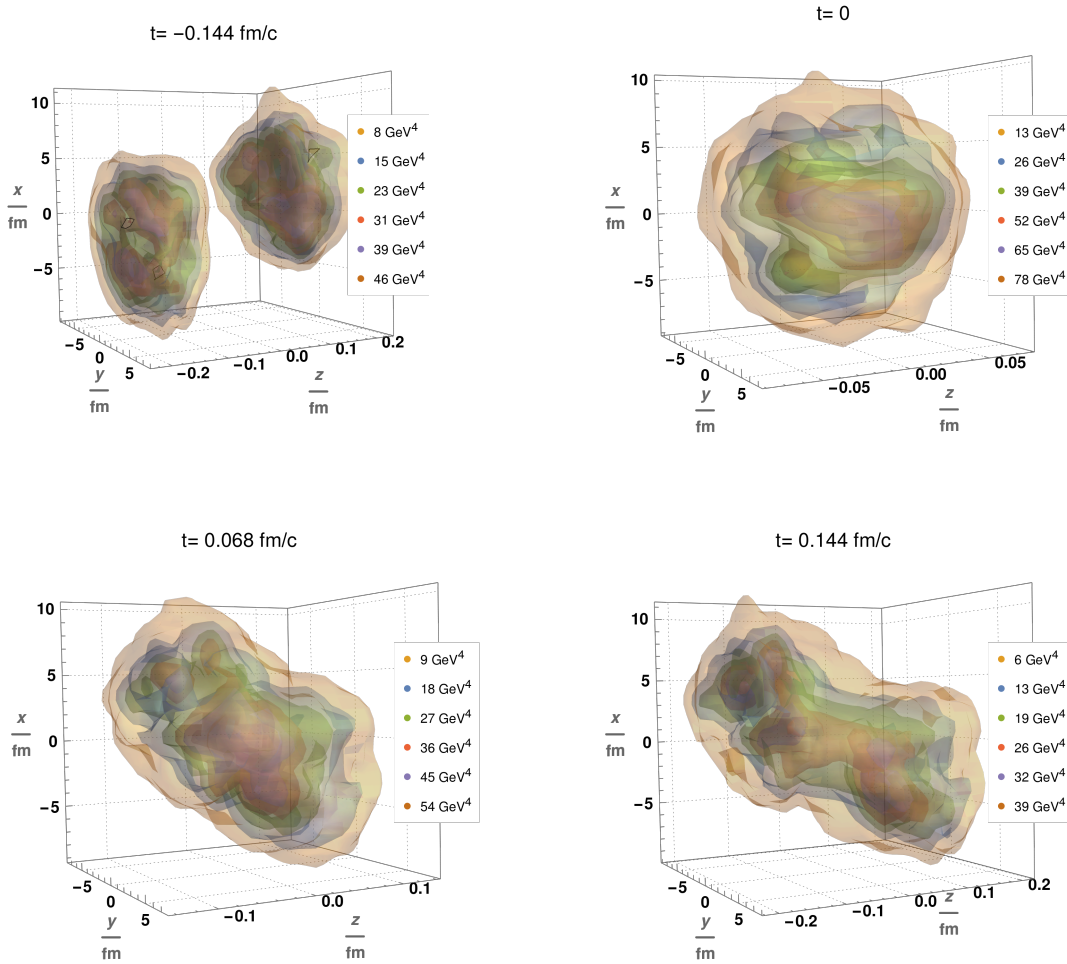


Figure 1: The energy density distribution during the collision of localized, granular, highly contracted holographic shocks computed up to first order in transverse derivatives. The spatial directions are labeled in units of [fm]. From top left to bottom right: the surface plots of the energy density evaluated at times $t = -0.144$ fm/ c , $t = 0$ fm/ c , $t = 0.068$ fm/ c , and $t = 0.144$ fm/ c .

density, respectively. Towards the endpoint of our time integration at time $t = 0.144$ fm/ c the energy density averaged over the central region ($|x_{\perp}| < 2.5$ fm) falls off with the approximate rate $\propto t^{-0.9}$, the same rate as observed during planar collisions. In Fig 2 and Fig. 3 we show the momentum density and the energy density at vanishing y coordinate, where \hat{y} is the transverse plane unit vector orthogonal to the impact parameter vector, on the same time slices as depicted in Fig. 1. Figure 4 shows the lab-frame angle-averaged transverse energy flux, $\langle T^{0\perp} \rangle \equiv \langle T^{0i}(\hat{x}^{\perp})^i \rangle$, as a function of

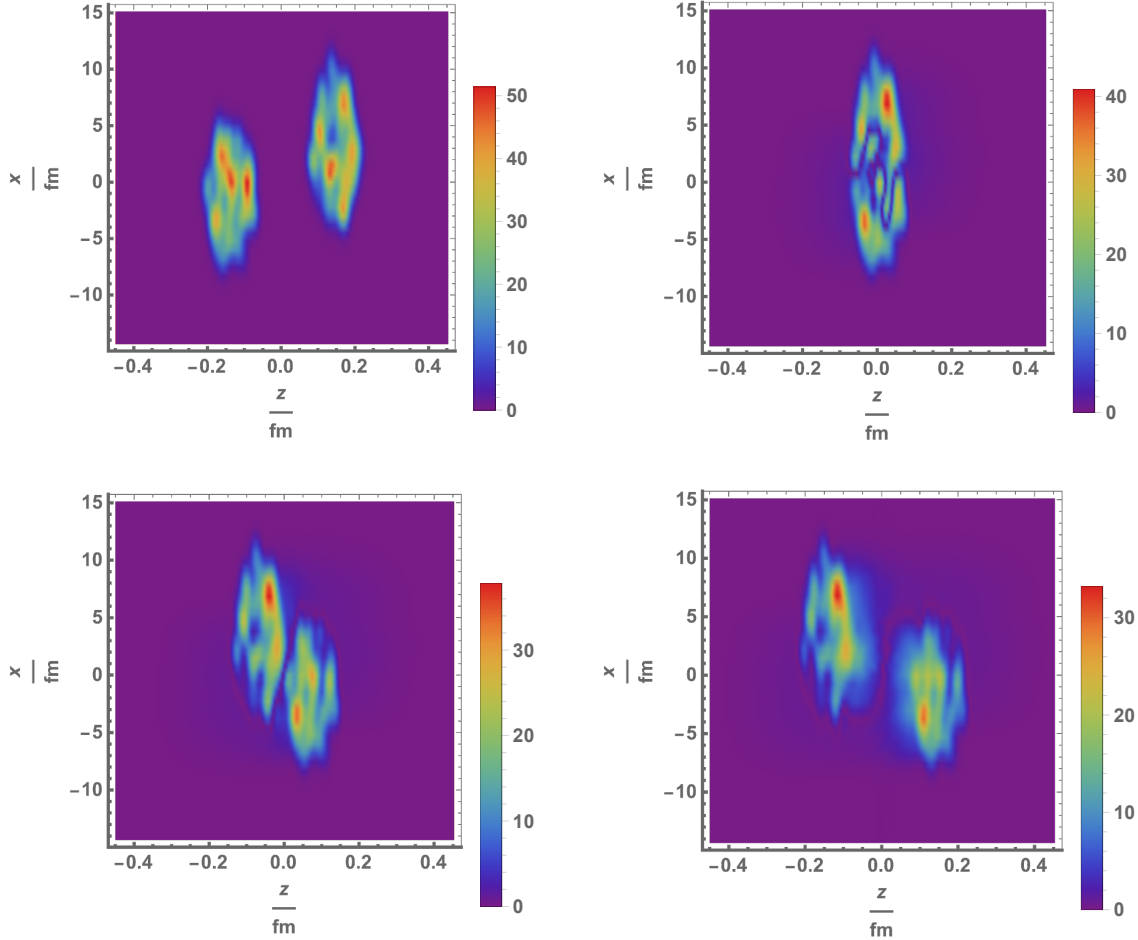


Figure 2: The absolute value of the energy flux $|T^{0i}|$ in units of $[\text{GeV}^4]$ as a function of the longitudinal coordinate z and the transverse coordinate x , at $y = 0$ and at various times. From top left to bottom right, the $y = 0$ slices depict the momentum density at $t = -0.144 \text{ fm}/c$, $t = 0 \text{ fm}/c$, $t = 0.068 \text{ fm}/c$ and $t = 0.144 \text{ fm}/c$.

the transverse radius $x_{\perp} \equiv \sqrt{x^2 + y^2}$. We also compare our results to previous ones for the transverse flow, where the granular structure of the projectiles had not been taken into account [1]. For this we matched the amplitudes $\sqrt{\mu_+(\mathbf{x}_{\perp}=0)\mu_-(\mathbf{x}_{\perp}=0)}$, where $\mu_{\pm}(\mathbf{x}_{\perp}=0)^3$ is the longitudinally integrated energy density at the central point of the right (+) and left (-) moving shocks. After this we rescale the transverse grid so that the transverse grid size in inverse units of $\sqrt{\mu_+(\mathbf{x}_{\perp}=0)\mu_-(\mathbf{x}_{\perp}=0)}$ in [16] matches the size chosen in this work. Zeroth order in transverse derivative terms are not affected by changing the transverse length. First order quantities such as $\langle T^{0\perp} \rangle$ scale as $\langle T^{0\perp} \rangle \rightarrow a^{-1} \langle T^{0\perp} \rangle$ if we rescale the transverse length $L_{\perp} \rightarrow aL_{\perp}$. Note that starting

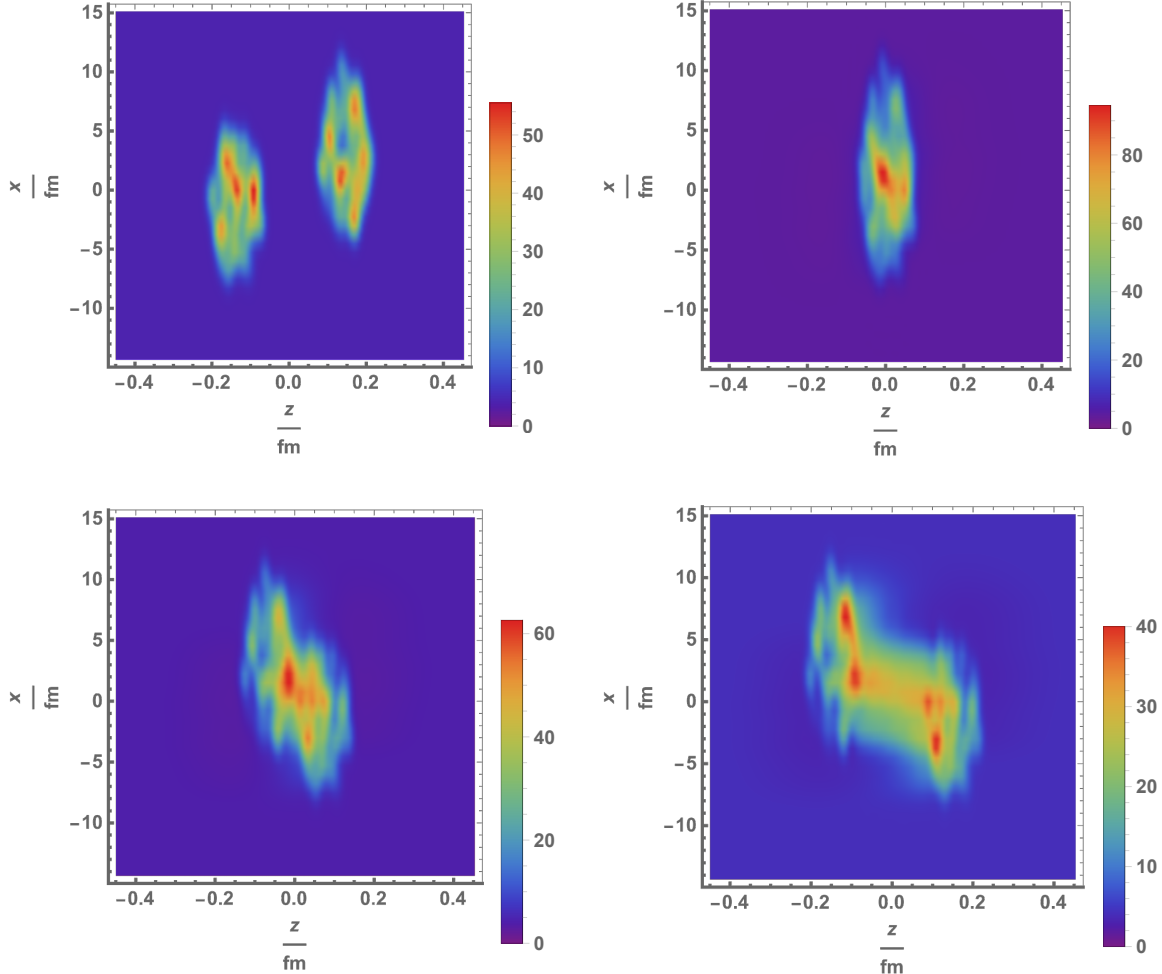


Figure 3: The energy density T^{00} in units of $[\text{GeV}^4]$ as a function of the longitudinal coordinate z and the transverse coordinate x , at $y = 0$ and at various times. From top left to bottom right, the $y = 0$ slices are evaluated at $t = -0.144 \text{ fm}/c$, $t = 0 \text{ fm}/c$, $t = 0.068 \text{ fm}/c$ and $t = 0.144 \text{ fm}/c$.

from a solution to the Einstein equations and rescaling both the amplitude and the transverse size, without changing the longitudinal size, does not in general generate a valid solution of the Einstein equations. Therefore, a priori it was not clear whether the results obtained in [1] can be used to approximate collisions with realistic aspect ratios of the colliding projectiles, corresponding to Lorentz contractions at RHIC, without showing that the disagreement between the first order in derivative approximation and exact results is small [16]. After these operations both the projectiles in [1, 16] and in this work have a similar overlap region, a similar longitudinal width and by construction the same amplitude, making this comparison possible. The yellow curves in Fig 4

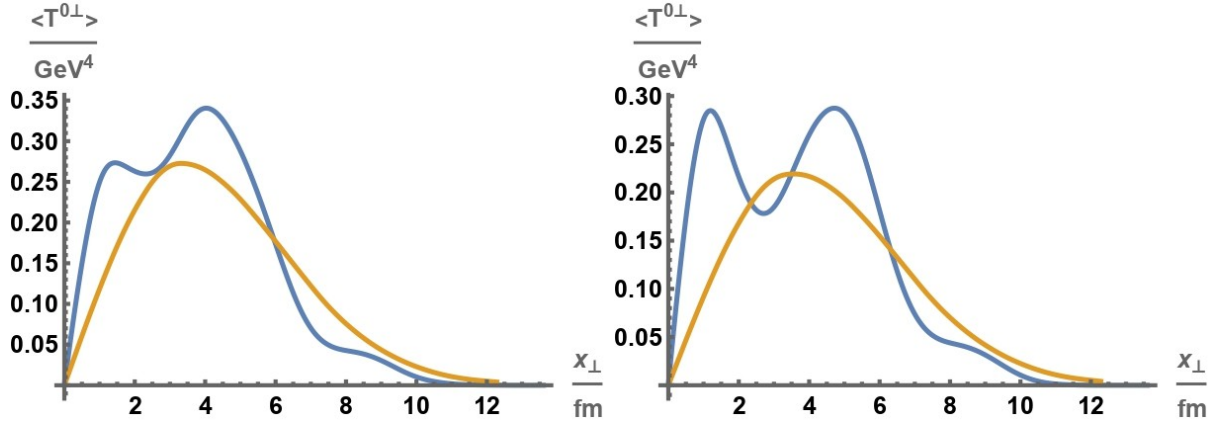


Figure 4: The transverse plane angle-averaged transverse momentum density $\langle T^{0\perp} \rangle \equiv \langle T^{0i}(\hat{x}^\perp)^i \rangle$ at rapidities $\xi = 0$ (left) and $\xi = 0.5$ (right), and at proper time $\tau = 0.1$ fm/ c . The blue curve corresponds to the results obtained in this work, starting from initial conditions (2.1) with left and right moving shocks given by (2.8). The yellow curves are obtained from extrapolating results in [1] using the fact that the difference between a first order in transverse derivative approximation and exact results for aspect ratios corresponding to those of Lorentz contracted projectiles at RHIC are small ($< 10\%$) [16].

represent the prediction of [1] for the transverse flow during the early phase after heavy ion collisions, using realistic parameters for the transverse extent and the amplitude of the shocks. The blue curves are the updated results computed in this work, using a Woods-Saxon potential as probability distribution for the individual nuclei and taking into account our particular realizations of the lumpy structure of the projectiles. While the maximum value and the compact support of the averaged transverse energy flux of the results in [1, 16] and the results presented in this work (that take into account the granular structure of the projectiles) are similar, the shape of $\langle T^{0\perp} \rangle$ as a function of x_{\perp} is noticeably affected by starting from lumpy instead of smooth initial conditions, despite the angle average.

4.2 Hydrodynamization

Comparing the stress energy tensor after the collision with its hydrodynamic approximation, where the constitutive relations are truncated after the first order in derivatives, allows one to quantify whether a hydrodynamic description of the dynamics is useful. At each order in the transverse derivative expansion we compute the fluid velocity from the eigenvalue equation

$$T^\mu{}_\nu u^\nu = -\varepsilon u^\mu, \quad (4.1)$$

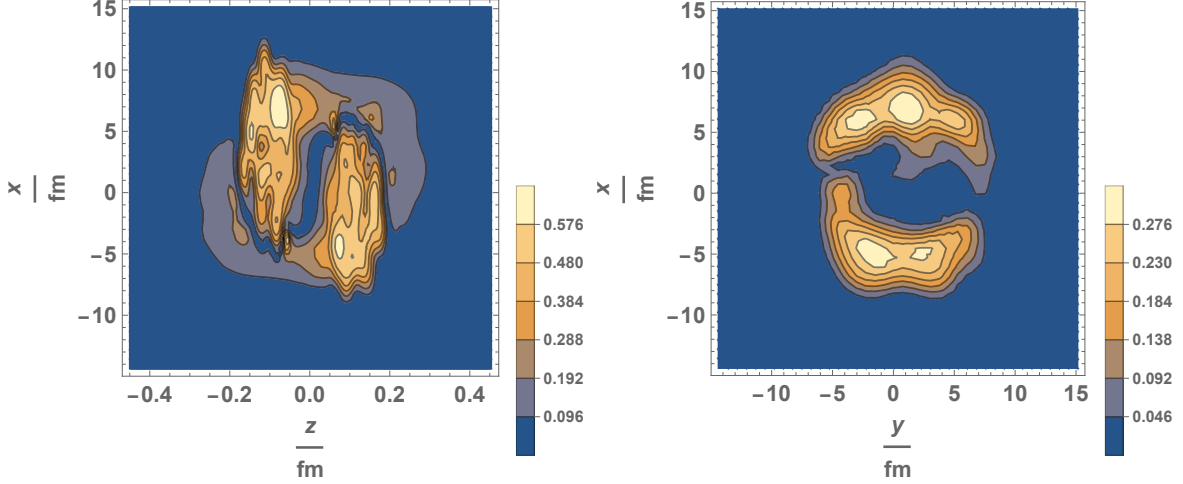


Figure 5: The absolute value of the fluid three velocity $|\mathbf{u}/u^0|$ at time $t = 0.1$ fm/ c . The left plot shows $|\mathbf{u}/u^0|$ at a $y = 0$ slice, the right plot shows it at a $z = 0$ slice.

where the eigenvalue ε is the proper energy density. The hydrodynamic approximation

$$\widehat{T}_{\text{hydro}}^{\mu\nu} = p g^{\mu\nu} + (\varepsilon + p) u^\mu u^\nu + \Pi^{\mu\nu}, \quad (4.2)$$

with the viscous stress Π given by

$$\Pi_{\mu\nu} = -2\eta \left[\partial_{(\mu} u_{\nu)} + u_{(\mu} u^\rho \partial_\rho u_{\nu)} - \frac{1}{3} \partial_\alpha u^\alpha (\eta_{\mu\nu} + u_\mu u_\nu) \right] + \mathcal{O}(\partial^2), \quad (4.3)$$

is also expanded up to first order in transverse derivatives. Here p is the pressure and η the shear viscosity.

We show slices of the fluid velocity three vector's absolute value $|\mathbf{u}/u^0|$ at time $t = 0.1$ fm/ c in Fig. 5. Next we compute the residual

$$\Delta = \frac{3}{\varepsilon} \sqrt{\Delta T^{\mu\nu} \Delta T_{\mu\nu}} \quad (4.4)$$

with $\Delta T^{\mu\nu} = T^{\mu\nu} - \widehat{T}_{\text{hydro}}^{\mu\nu}$. Following earlier work [1, 2, 4], $\Delta < 0.15$ is regarded as the onset of approximate validity of hydrodynamics. As shown in [16], first order corrections to the residual Δ are negligible. However, explicitly computing first order in transverse derivative corrections of the fluid velocity from Eq. (4.1) is necessary for determining the vorticity (up to first order in transverse gradients), which is discussed in the next section.

We show the results for Δ in Fig. 6. As can be seen there, most of the low rapidity ($\xi \approx 0$) central region can be described by hydrodynamics at $\tau = 0.1$ fm/ c , but only a small subset of the plasma at mid-rapidity ($|\xi| \approx 0.5$) has hydrodynamized at this

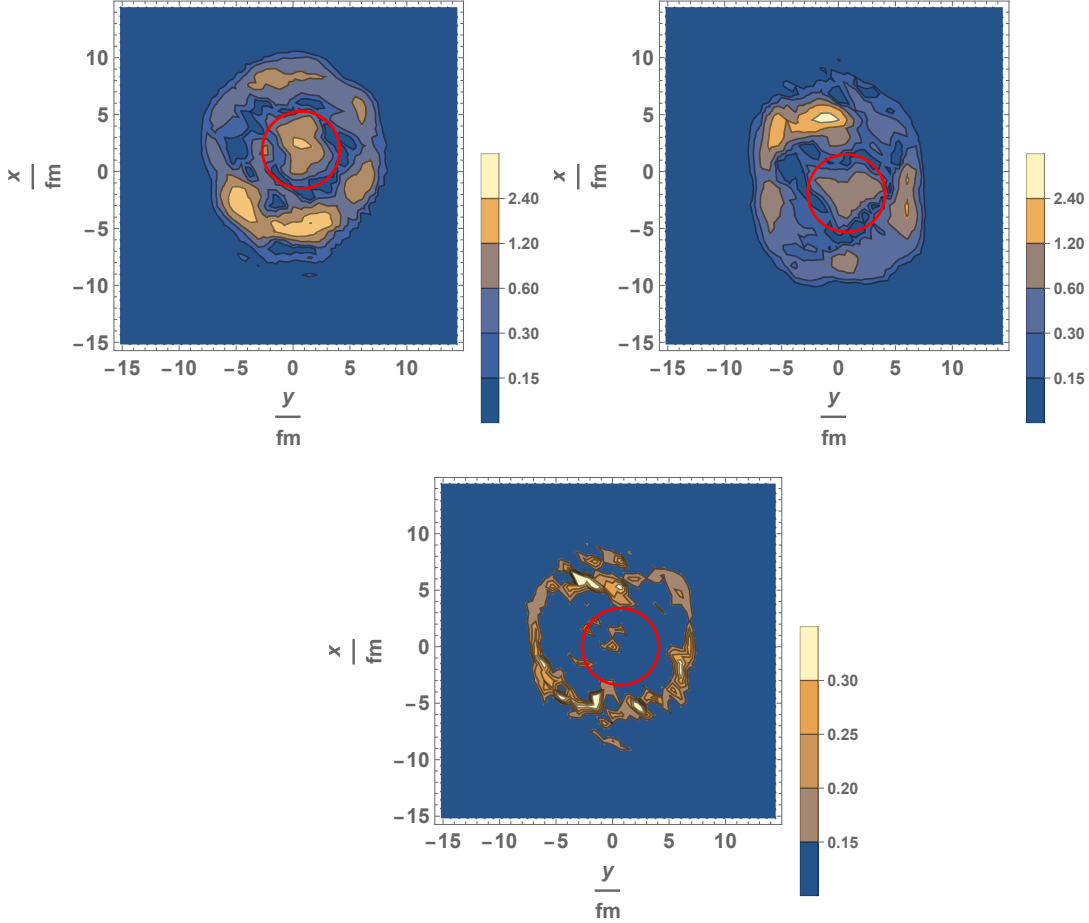


Figure 6: The residual Δ at proper time $\tau = 0.106 \text{ fm}/c$. For rapidity $\xi = -0.5$ (left) and $\xi = 0.5$ (right) in the first row and vanishing rapidity for the plot in the second row. We display the region \mathcal{R} described in (4.5) by a red circle in the plots above.

proper time. In order to provide initial data for hydro evolutions on a full initial hypersurface, one would have to evolve the geometry substantially longer, which goes beyond the scope of this work. At time $t \approx 0.1 \text{ fm}/c$ after the collision, the majority of the plasma around the central point $\mathbf{x}_\perp = 0, z = 0$ is hydrodynamized. We depict this behavior in Fig. 7, where we show the median of the hydro residual Δ in the central regions $|x_\perp| < 1.5 \text{ fm}$ and $|x_\perp| < 7.5 \text{ fm}$ both at rapidity $\xi = 0$ and at rapidity $\xi = 0.25$ as a function of proper time. As shown there at proper time $\tau \approx 0.1 \text{ fm}/c$, the majority of the low rapidity plasma in the central region has hydrodynamized, while even at vanishing rapidity individual transverse pixels can still be far from the hydrodynamic approximation, as shown in Fig. 6. Nonetheless, we can attempt to identify the early

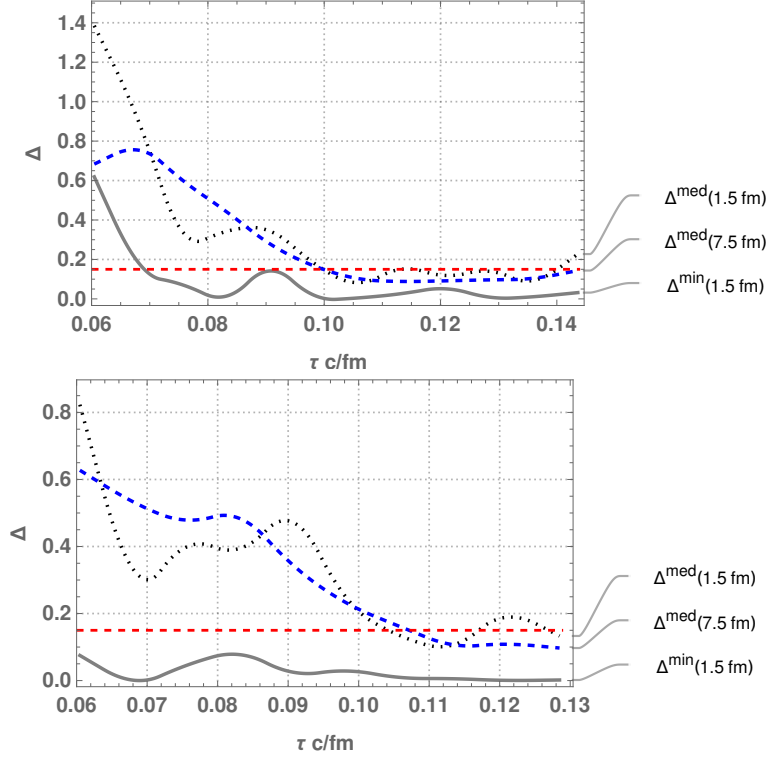


Figure 7: In the top plot we show the median hydro residual at rapidity $\xi = 0$. The red dashed line corresponds to $\Delta = 0.15$. The black dotted line shows the residual averaged over the central region $|x_{\perp}| < 7.5$ fm, whereas the blue dashed curve shows the same for $|x_{\perp}| < 1.5$ fm. The gray line shows the minimal Δ in the region $|x_{\perp}| < 1.5$ fm. The plot below depicts the analogous functions at rapidity $\xi = 0.25$.

proper time part of the hydrodynamization surface: In the immediate neighborhood of the tube or thin pipe shaped subregion \mathcal{R} defined at constant proper time $\tau = 0.106$ fm/ c via

$$\mathbf{x}_{\perp} = \{-3.8\xi + 3.4 \cos(\phi), 0.7 + 3.4 \sin(\phi)\}, \quad (4.5)$$

for $\phi \in [0, 2\pi]$ and $|\xi| < 0.5$, the median hydro residual is already below the threshold $\Delta < 0.15$. The red circle in Fig. 6 shows slices of this region \mathcal{R} at $\tau = 1.06$. It should be noted that, due to the strong inhomogeneity of the hydro residual Δ , statements about the exact hydrodynamization time can only be made locally or by averaging. They generally depend on the specific spatial region that is considered. The origin of this inhomogeneity is well understood: As observed in [4, 6], the hydrodynamization proper time of the plasma located at a transverse pixel is proportional to the inverse geometric mean of the longitudinally integrated energy densities of the two initial projectiles

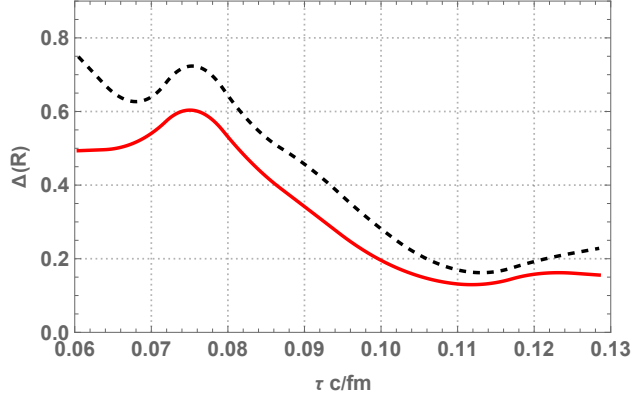


Figure 8: The hydro residual $\Delta(\mathcal{R})$ averaged over the region \mathcal{R} as a function of proper time τ (black, dashed curve) and the median Δ in the region \mathcal{R} (red solid line).

evaluated at the transverse coordinate of this pixel. Thus the hydro residual Δ reflects the strong transverse fluctuations of the initial data. In Fig. 8 we depict both the average and the median hydro residual Δ in the region R as a function of proper time. At proper time $\tau = 1.06$ fm/ c the averaged hydro residual has dropped to 0.19, whereas the median is at 0.14. In summary, the median of the hydro residual Δ in the central region (shown in Fig. 7) drops below 0.15 at time $t = 0.1$ fm/ c which, in units of the longitudinally integrated energy density of the central region μ^3 , corresponds to $t = 1.4/\mu$, and is therefore close to the hydrodynamization time of the central region found in [2] without granular initial data, which was $t \approx 1.25/\mu$. However, the hydrodynamization time of individual pixels varies drastically due to the influence of the granular structure on the local energy density scale, as is clearly evident from the variation in the hydro residual Δ shown in Fig. 6. This is in line with expectation of earlier works [24] which predicted a substantial delay (by roughly a factor of 2) of the hydrodynamization of the full system due to the granular structure. We show the fluid velocity and the proper energy density in the region \mathcal{R} as function of the angle ϕ and the rapidity ξ in Fig. 9. One sees that the transverse velocity in this region is quite modest, $|\vec{u}_\perp| \lesssim 0.02$ while the longitudinal velocity component is substantial, $|u_z| \sim 0.25$ at rapidity $\xi = \pm 0.5$.

4.3 Vorticity

Examining the vorticity of the produced quark gluon plasma is interesting. There has been much discussion of how the plasma vorticity, when evolved through to hadronization, may leave signatures in the polarization of measured Λ hyperons [27]. Recent advances in hydrodynamics [28], which now allow one to incorporate a spin chemical

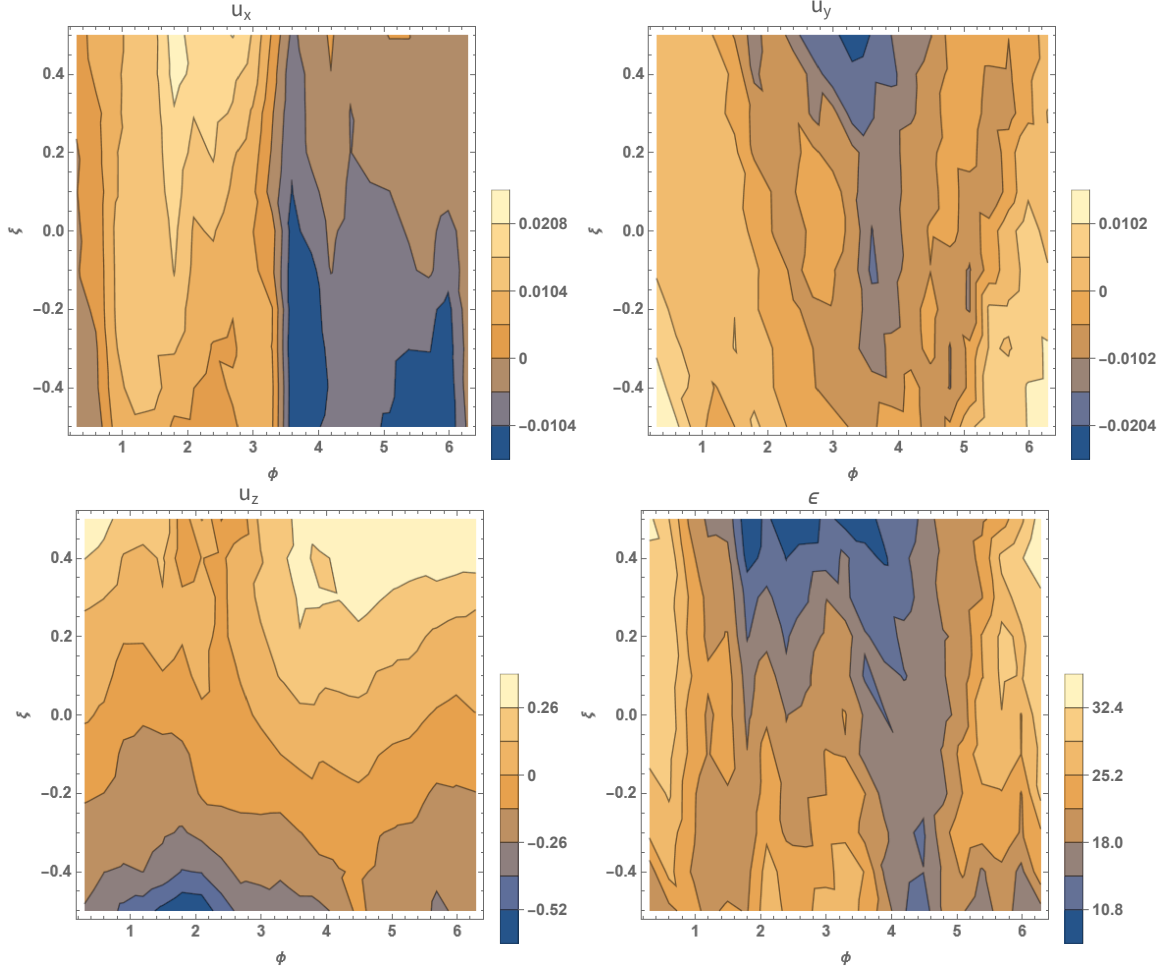


Figure 9: The fluid velocity and the proper energy density in the hydro-subregion \mathcal{R} defined in (4.5) as a function of rapidity ξ and ϕ given in (4.5). The first row corresponds to the transverse fluid velocity with u_x corresponding the left and u_y to the right plot. The second row shows the longitudinal fluid velocity u_z on the left and the proper energy density, which is given in units of $[\text{GeV}^4]$, on the right.

potential into hydrodynamic evolution, open up the possibility of clarifying to what extent vorticity is responsible for the observed polarization, starting from the boosted, nuclear heavy ion model described previously and following the evolution of vorticity throughout the collision using holographic modeling of pre-hydrodynamic dynamics followed by hydrodynamic evolution thereafter. With this motivation in mind we examine the vorticity

$$\omega^\alpha \equiv -\frac{1}{2} \epsilon^{\alpha\beta\gamma\delta} u_\delta \partial_\beta u_\gamma \quad (4.6)$$

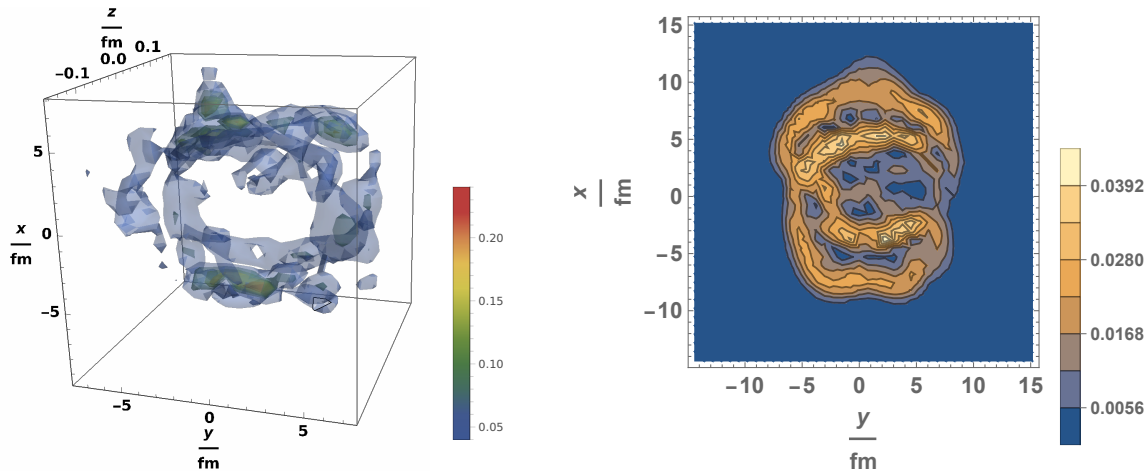


Figure 10: On the left: The absolute value of the vorticity three vector $\vec{\omega}$ at $t = 0.1$ fm/c, the spatial coordinates on the axes are given in units of [fm]. On the right we show the vorticity at $t = 0.1$ fm/c at vanishing rapidity. The results are given in units of [GeV]. Most of the initial (geometric) angular momentum is deposited far away from the central region where the hydrodynamized quark gluon plasma is located.

of the early quark gluon plasma at the time when the majority of the central, low rapidity region has hydrodynamized. In Fig. 10 we show the absolute value of the vorticity three vector $|\vec{\omega}|$, with $\omega^\alpha = (\omega^0, \vec{\omega})$, at $t = 0.1$ fm/c. We find that almost none of the large, initial spatial vorticity $|\vec{\omega}|$ is deposited in the central, hydrodynamized region of the quark gluon plasma. In other words, the plasma is only slowly rotating despite the large, initial “geometric” angular momentum in the system arising from a large impact parameter. In Fig. 11 we show the median vorticity in the central regions $|x_\perp| < 1.5$ fm and $|x_\perp| < 7.5$ fm, the same regions for which we presented the averaged hydro residual Δ in Fig. 7. Likewise, in analogy to Fig. 8 which shows the hydro residual in the region \mathcal{R} , we depict the average and median vorticity in the region \mathcal{R} in Fig. 12.

There has also been discussion about the relation between the mean spin vector, and thus the polarization of emitted spin $\frac{1}{2}$ particles, and the “thermal vorticity,” defined as

$$\bar{\omega}_{\mu\nu} \equiv \frac{1}{2} \left(\partial_\mu \beta_\nu - \partial_\nu \beta_\mu \right), \quad (4.7)$$

where $\beta^\mu = u^\mu/T$ with the (local) temperature T inferred from the local energy density. The authors of [29] proposed a relation

$$S^\mu(x, p) \sim (1 - n_F) \epsilon^{\mu\nu\rho\sigma} p_\nu \bar{\omega}_{\rho\sigma} + \mathcal{O}(\bar{\omega}^2) \quad (4.8)$$

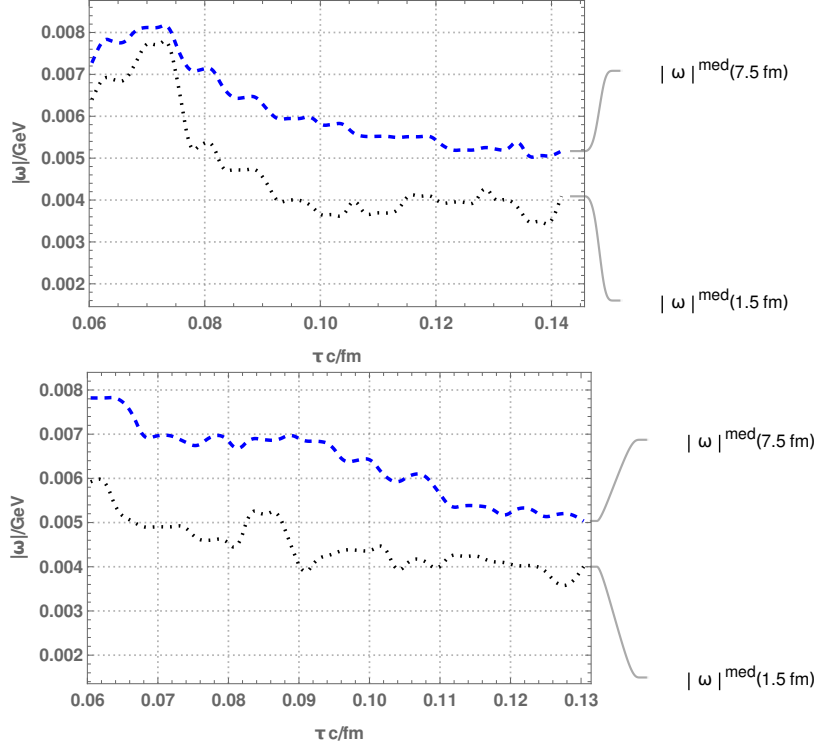


Figure 11: In the top plot we show the median absolute value of the three vector vorticity $|\vec{\omega}|$, given by the spatial components of (4.6) at rapidity $\xi = 0$. The black dotted line shows the vorticity averaged over the central region $|x_{\perp}| < 7.5$ fm, whereas the blue dashed curve shows the same for $|x_{\perp}| < 1.5$ fm. The plot below depicts the analogous functions at rapidity $\xi = 0.25$. Even at proper times the average vorticity in the central, low rapidity region is only about 2% of the peak vorticity.

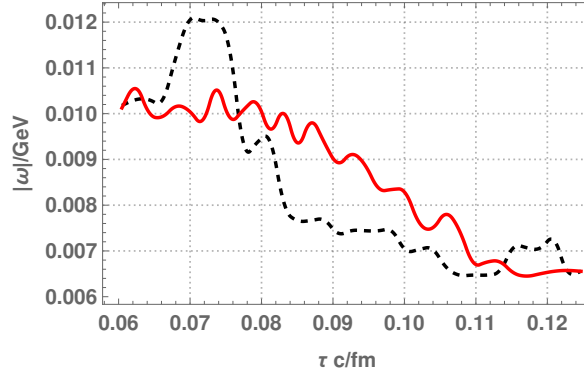


Figure 12: The median (red solid curve) and the average (black dashed curve) absolute spatial vorticity $|\vec{\omega}|$ in the region \mathcal{R} defined in (4.5) as a function of proper time.

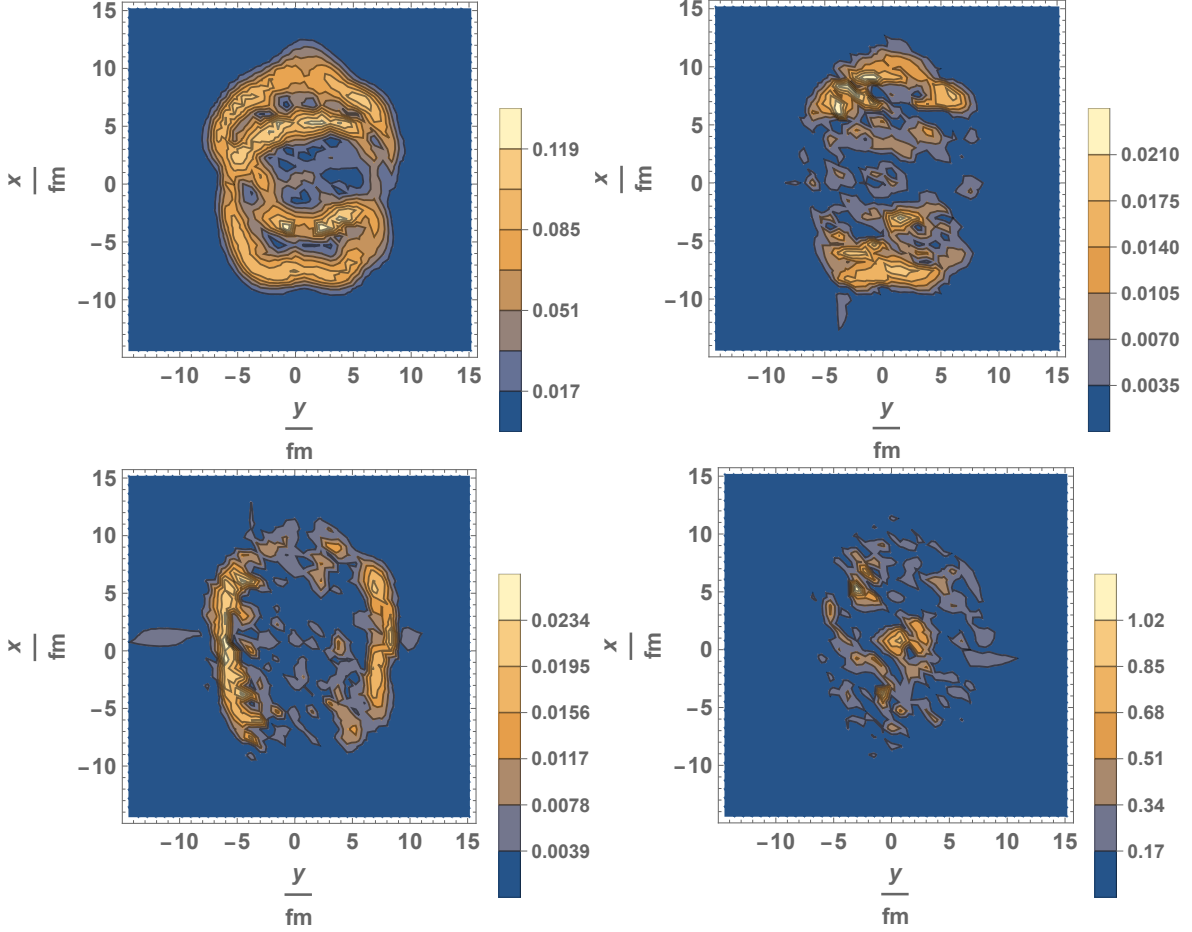


Figure 13: Top left: The absolute value of the spatial components ($\bar{\omega}^{yz}, \bar{\omega}^{xz}, \bar{\omega}^{xy}$) of the thermal vorticity $\bar{\omega}^{\mu\nu}$, on the central plane $z = 0$. Top right: The absolute value of $\bar{\omega}^{tx}$. Bottom left: The absolute value of $\bar{\omega}^{ty}$. Bottom right: The absolute value of $\bar{\omega}^{tz}(= -\bar{\omega}^{zt})$, which is the only non-negligible $\bar{\omega}$ component of the thermal vorticity at the center of the hydrodynamized part of the plasma. All plots display results at $t = 0.1$ fm/ c and are given in units of [GeV].

between the thermal vorticity $\bar{\omega}$ and the mean spin vector $S^\mu(x, p)$ and four-momentum p_ν of an emitted particle (with n_F the Fermi-Dirac distribution). While this relation is, at best, relevant on the freeze-out surface, this suggestion motivates us to examine the early development of the so-defined thermal vorticity. Fig. 13 shows the size of components of the thermal vorticity $\bar{\omega}^{\mu\nu}$ at the central plane $z = 0$.

We find that $\bar{\omega}^{tz}(= -\bar{\omega}^{zt})$ is the only component of significant size in the central region at the time when the majority of this region has hydrodynamized, $t \approx 0.1$ fm/ c . The dominant contribution to $\bar{\omega}_{tz}$ originates from the time derivative of the

longitudinal fluid velocity $\partial_t u_z$, which is large compared to transverse components of the fluid velocity. In an idealized setting of perfectly smooth, Gaussian projectiles, the u_z component vanishes at the central point, due to the exact anti-symmetry of u_z in the longitudinal z direction with respect to the origin. However, due to the lumpy structure of our initial data this no longer holds exactly.

5 Conclusion

Solving the Einstein equations, using a truncated expansion in transverse derivatives, we have numerically calculated, via gauge/gravity duality, the collision of two highly boosted, lumpy, localized distributions of energy density in $\mathcal{N} = 4$ super Yang-Mills theory. To model heavy ion collisions, we craft our gravity initial data to correspond to a state in the boundary field theory whose stress-energy expectation value matches a reasonably realistic model of highly boosted and Lorentz contracted heavy ions. The parameters we chose reflect those used in prior modeling of RHIC collisions. This is the first attempt to use holographic methods to directly investigate the influence of the nuclear structure of heavy ions on the post-collision flow. We limited our (real world) computation time to about three weeks, during which we computed the collision dynamics up until $t = 0.144 \text{ fm}/c$ (with $t = 0$ corresponding to the time when the longitudinal positions of the projectiles' centers of mass coincide). We studied the hydrodynamization time of the central collision region and found only a modest delay compared with results that do not incorporate the lumpy structure of the projectiles: In units of the third root of the longitudinally integrated energy density μ , a hydrodynamization time of the low rapidity, central region of $t_{hydro} \approx 1.25 \mu$ was found in [1], using analogous units we find that more than half of the the low rapidity, central region is hydrodynamized at time $t_{hydro} \approx 1.4 \mu$. However, individual transverse plane pixels in the central, low rapidity region are still far from a hydrodynamic description, which is in line with expectations of [24].

We found that the hydrodynamized part of the plasma is only slowly rotating despite the large, initial, “geometric” angular momentum. The only sizable contributions to the thermal vorticity came from relativistic corrections. The small vorticity we find early after the collision in the hydrodynamized region makes it highly unclear whether subsequent hydrodynamic evolution, up until the freeze-out surface, will yield a vorticity that is sizable enough to account for the observed polarization of emitted Λ hyperons.

In future work, we hope to extend the evolution further in time, long enough to capture the entire hydrodynamization hypersurface and use the stress energy tensor on this surface as initial data for subsequent hydro evolutions. Moreover, it will be

very interesting to consider holographic collisions including a proper treatment of electromagnetism and the spatially distributed charge and current densities, and thereby incorporate the effects of the strong but transient magnetic background field which develops during heavy ion collisions and study its effect on the dynamics. Further future directions include computing localized collisions including finite coupling corrections [31–33], and solving analogous problems in holographic models closer to QCD.

Acknowledgments

The work of LY was supported by the U.S. Department of Energy grant DE-SC-0011637. SW acknowledges support by an Israeli Science Foundation excellence center grant 2289/18 and a Binational Science Foundation grant 2016324. Parts of the work of SW were supported by the U.S. Department of Energy grant DE-SC-0011637 and the Feodor Lynen fellowship program of the Alexander von Humboldt foundation.

Appendix: Transverse derivative expansion

We give a short overview of the approximation scheme, following [16], that we used to calculate the holographic collisions. Exploiting the large disparity between longitudinal and transverse scales during heavy ion collisions, we effectively replace transverse derivatives $\partial_\perp \rightarrow \epsilon \partial_\perp$, expand the Einstein equations in powers of ϵ , solve them order by order, and then set $\epsilon = 1$ at the end.

Let us write the Einstein equations for a metric G schematically as

$$E(G) = 0. \tag{5.1}$$

Expanding in transverse derivatives, we have

$$E(G) = E^{(0)}(G) + \epsilon E^{(1)}(G) + \epsilon^2 E^{(2)}(G), \tag{5.2}$$

where the differential operator $E^{(i)}$ contains i powers of transverse derivatives. Let $G_{\mu\nu}^{(i)}$ denote an approximate solution to the Einstein equations valid to order $\mathcal{O}(\epsilon^i)$ so that

$$E(G^{(i)}) = \mathcal{O}(\epsilon^{i+1}). \tag{5.3}$$

At the lowest order $G_{\mu\nu}^{(0)}(x^0, x^\parallel, \mathbf{x}^\perp)$ is, for every fixed value of \mathbf{x}^\perp , some solution to the planar Einstein equations (obtained by neglecting transverse derivatives), with parameters of the specific planar solution varying slowly with x^\perp . At zeroth order

$$E^{(0)}(G^{(0)}) = 0. \tag{5.4}$$

One now systematically corrects this zeroth order approximation by writing

$$G_{\mu\nu}^{(i)}(x^0, x^\parallel, \mathbf{x}^\perp) = G_{\mu\nu}^{(i-1)}(x^0, x^\parallel, \mathbf{x}^\perp) + \delta g_{\mu\nu}^{(i)}(x^0, x^\parallel, \mathbf{x}^\perp) \quad (5.5)$$

and demands that the Einstein equations hold up to the next order. Let $\Delta_L^{(i)}$ be the planar Lichnerowicz operator evaluated on $G^{(i)}$,

$$\Delta_L^{(i)} \equiv \frac{\delta E^{(0)}(G^{(i)})}{\delta G^{(i)}}. \quad (5.6)$$

Then Eq. (5.3) will be satisfied if

$$\Delta_L^{(i-1)} \delta g^{(i)} = -E^{(0)}(G^{(i-1)}) - \epsilon E^{(1)}(G^{(i-1)}) - \epsilon^2 E^{(2)}(G^{(i-2)}). \quad (5.7)$$

See [16] for a more detailed exposition.

References

- [1] P. M. Chesler and L. G. Yaffe, *Holography and off-center collisions of localized shock waves*, *JHEP* **1510**, 070 (2015), [arXiv:1501.04644](#)
- [2] P. M. Chesler and L. G. Yaffe, *Numerical solution of gravitational dynamics in asymptotically anti-de Sitter spacetimes*, *JHEP* **1407**, 086 (2014), [arXiv:1309.1439](#)
- [3] P. M. Chesler, L. G. Yaffe, *Holography and colliding gravitational shock waves in asymptotically AdS₅ spacetime*, *Phys. Rev. Lett.* **106**, 021601 (2011), [arXiv:1011.3562](#)
- [4] P. M. Chesler, N. Kilbertus and W. van der Schee, *Universal hydrodynamic flow in holographic planar shock collisions*, *JHEP* **1511**, 135 (2015), [arXiv:1507.02548](#) [hep-th].
- [5] J. Casalderrey-Solana, M. P. Heller, D. Mateos and W. van der Schee, *From full stopping to transparency in a holographic model of heavy ion collisions*, *Phys. Rev. Lett.* **111**, 181601 (2013), [arXiv:1305.4919](#) [hep-th].
- [6] S. Waeber, A. Rabenstein, A. Schäfer, L. G. Yaffe, *Asymmetric shockwave collisions in AdS₅*, *JHEP* **1908**, 005 (2019), [arXiv:1906.05086](#) [hep-th]
- [7] W. van der Schee, B. Schenke, *Rapidity dependence in holographic heavy ion collisions*, *Phys. Rev. D.* **92**, 064907 (2015), [arXiv:1507.08195](#) [hep-th]
- [8] W. van der Schee, P. Romatschke, S. Pratt, *A fully dynamical simulation of central nuclear collisions*, *Phys. Rev. D.* **111**, 222302 (2013), [arXiv:1307.2539](#) [hep-th]
- [9] J. Casalderrey-Solana, D. Mateos, W. van der Schee, M. Trianae, *Holographic heavy ion collisions with baryon charge*, *JHEP* **1609**, 108 (2016), [arXiv:1607.05273](#) [hep-th]

- [10] B.Alver, M.Baker, C.Loizides, P.Steinberg, *The PHOBOS Glauber Monte Carlo*, [arXiv:0805.4411](#) [nucl-ex]
- [11] C. Loizides, J. Nagle, P. Steinberg, *Improved version of the PHOBOS Glauber Monte Carlo*, (2014), 10.1016/j.softx.2015.05.001, [arXiv:1408.2549](#) [nucl-ex]
- [12] L. McLerran, R. Venugopalan *Gluon distribution functions for very large nuclei at small transverse momentum*, *Phys. Rev. D* **49**, 3352 (1994), [arXiv:hep-ph/9311205](#)
- [13] J. E. Bernhard, J. S. Moreland, S. A. Bass, J. Liu, U. Heinz, *Applying Bayesian parameter estimation to relativistic heavy-ion collisions: simultaneous characterization of the initial state and quark-gluon plasma medium*, *Phys. Rev. C* **94**, 024907 (2016), [arXiv:1605.03954](#) [nucl-th]
- [14] ALICE collaboration, *Anisotropic flow of identified particles in Pb-Pb collisions at $\sqrt{s_{NN}} = 5.02$ TeV*, *JHEP* **1809**, 006 (2018), [arXiv:1805.04390](#) [nucl-ex]
- [15] S. Voloshin, Y. Zhang, *Flow study in relativistic nuclear collisions by Fourier expansion of azimuthal particle distributions*, *Zeitschrift für Physik C Particles and Fields*, volume 70, pages 665–671 (1996), [arXiv:hep-ph/9407282](#)
- [16] S. Waeber, L. G. Yaffe, *Collision of localized shocks in AdS_5 as a series expansion in transverse gradients*, [arXiv:2206.01819](#) [hep-th]
- [17] H. De Vries, C.W. De Jager, and C. De Vries, *Atom. Data Nucl. Data Tabl.* **36** 495 (1987)
- [18] C.W. de Jager, H. de Vries, and C. de Vries, *nuclear charge- and magnetization-density-distribution from elastic electron scattering*, *Atomic Data and Nuclear Data Tables* 14 (1974) 485.
- [19] S. Bhattacharyya, V. E. Hubeny, S. Minwalla, M. Rangamani, *Nonlinear fluid dynamics from gravity*, *JHEP* **0802**, 045 (2008), [arXiv:0712.2456](#)
- [20] H. Bondi, *Gravitational waves in general relativity*, *Nature* **186** (1960) no.4724, 535.
- [21] R. K. Sachs, *Gravitational waves in general relativity. 8. Waves in asymptotically flat space-times*, *Proc. Roy. Soc. Lond. A* **270** (1962) 103.
- [22] J. P. Boyd, *Chebyshev and Fourier Spectral Methods (Revised)*, Dover Books on Mathematics, Dover Publications, 2001
- [23] J. Vredevoogd, S. Pratt, *Universal flow in the first stage of relativistic heavy ion collisions*, *Phys. Rev. C* **79**, 044915 (2009), [arXiv:0810.4325](#) [nucl-th].
- [24] B. Müller, A. Rabenstein, A. Schäfer, S. Waeber, L. G. Yaffe, *Phenomenological implications of asymmetric AdS_5 shockwave collision studies for heavy ion physics*, *Phys. Rev. D* **110**, 211601 (2020), [arXiv:2001.07161](#) [hep-ph]

- [25] C. Ecker, D. Grumiller, P. Stanzer, S. A. Stricker, W. van der Schee, *Exploring nonlocal observables in shock wave collisions*, *JHEP* **1611**, 054 (2016), [arXiv:1609.03676](#) [hep-th]
- [26] J. Casalderrey-Solana, M. P. Heller, D. Mateos, W. van der Schee, *Longitudinal coherence in a holographic model of asymmetric collisions*, *Phys. Rev. Lett.* **112**, 221602 (2014), [arXiv:1312.2956](#)
- [27] STAR collaboration, *Global Λ hyperon polarization in nuclear collisions: evidence for the most vortical fluid*, *Nature* **548**, 62 (2017), [arXiv:1701.06657](#) [nucl-ex]
- [28] D. Gallegos, U. Gürsoy, A. Yarom, *Hydrodynamics of spin currents*, *SciPost Phys.* **11**, 041 (2021), [arXiv:2101.04759](#) [hep-th]
- [29] F. Becattini, V. Chandra, L. Del Zanna, E. Grossi *Relativistic distribution function for particles with spin at local thermodynamical equilibrium*, *Annals of Physics*, Volume **338**, p. 32-49., [arXiv:1303.3431](#) [nucl-th]
- [30] G. Giacalone, B. Schenke, C. Shen, *Constraining the nucleon size with relativistic nuclear collisions*, *Phys. Rev. Lett.* **128**, 042301 (2022), [arXiv:2111.02908](#) [nucl-th]
- [31] S. S. Gubser, I. R. Klebanov, A. A. Tseytlin, *Coupling Constant Dependence in the Thermodynamics of $N=4$ Supersymmetric Yang-Mills Theory*, *Nucl.Phys.B* **534**: 202-222, 1998, [arXiv:hep-th/9805156](#)
- [32] J. Pawelczyk, S. Theisen, *$AdS_5 \times S^5$ Black Hole Metric at $\mathcal{O}(\alpha'^3)$* , *JHEP* **9809**, 010 (1998), [arXiv:hep-th/9808126](#)
- [33] Å. Folkestad, S. Grozdanov, K. Rajagopal, W. van der Schee, *Coupling Constant Corrections in a Holographic Model of Heavy Ion Collisions with Nonzero Baryon Number Density*, *JHEP* **1912**, 093 (2019), [arXiv:1907.13134](#) [hep-th]